Research Article | Vol. 33, No. 15 / 28 Jul 2025 / Optics Express 32386
Optics EXPRESS

Research on impact of range resolutions on wind detection performance using virtual lidar

JIAXIU LIU,[1] JINLONG YUAN,[1,*] HAOYU YANG,[1] ANNING CHEN,[1] YUANHAO GU,[1] TIANWEN WEI,[1] AND HAIYUN XIA[1,2]

[1]School of Atmospheric Physics, Nanjing University of Information Science and Technology, Nanjing 210044, China
[2]School of Earth and Space Science, University of Science and Technology of China, Hefei 230026, China
[*]yuanjinlong@nuist.edu.cn

Abstract: The impact of range resolution on the accuracy of wind lidar cannot be ignored, which is quantitatively evaluated using virtual lidar. This study conducts a comparative analysis of three virtual lidar generation methods: the direct averaging method, the energy weighting method, and the time-domain analysis method. The error assessment between the wind retrieved by virtual lidar and the reference wind is carried out. Results show that insufficient range resolution can cause underestimation and misalignment of wind speed extremes. Moreover, there are differences in the retrieval results generated by the three virtual lidar methods. Based on these findings, a dimensionless parameter is proposed to decouple the relationship between range resolution and wind field scale. The fitting relationships between this parameter and error metrics are established, enabling the selection of the optimal virtual lidar generation method for different scenarios. Finally, wind speed errors and image similarity metrics are combined to comprehensively evaluate the impact of range resolutions on detection of typical building wake flow. This research provides a vital foundation for evaluating the wind field detection performance of coherent Doppler wind lidar, which remains applicable to direct detection wind lidar.

1. Introduction

Coherent Doppler wind lidar (CDWL), due to its high spatiotemporal resolution, high precision, and extensive detection range, has been widely applied in fields such as aviation safety [1–4], wind energy development [5,6], and atmospheric pollution [7,8]. In recent years, there has been continuous progress in the hardware systems [9,10] and inversion algorithms [11] of CDWL. However, many issues remain, particularly the issue of insufficient range resolution.

The mutual restriction between range resolution and detection distance makes it difficult to achieve an effective combination of fine-scale and wide-range detection. Insufficient range resolution poses significant challenges when attempting to detect the fine structure of small-scale wind fields [12]. When the range resolution is significantly lower than the wind field scale, it can lead to an underestimation of wind shear, thereby affecting the accuracy and reliability of the detection results. Currently, wind field detection error assessment of lidar primarily is based on the analysis of lidar signal-to-noise ratio (SNR) [13,14] and inversion algorithms [15,16]. The limitation of this assessment method is that it does not fully consider the impact of insufficient range resolution on the measurement results, leading to inaccurate error assessment. Therefore, the specific impact of range resolution on the detection performance of wind field at different scales is still an urgent issue that needs to be addressed. However, the system design, purchase and field experiment cost of CDWL are relatively high. The virtual lidar is expected to solve this problem.

The virtual wind lidar or lidar simulation technology offers an economical and effective solution to these issues. Currently, virtual wind lidar plays a crucial role in lidar system design,

#562053 https://doi.org/10.1364/OE.562053
Journal © 2025 Received 12 Mar 2025; revised 3 Jul 2025; accepted 8 Jul 2025; published 24 Jul 2025

Optics EXPRESS

experimental scheme optimization, and algorithm advancement [17–19]. It enables the testing and verification of various system configurations and scanning strategies in a simulated environment, aiding in the optimization of real lidar performance and applications, significantly reducing research costs and risks [20,21]. For example, virtual lidar provides comprehensive, customized solutions and services for complex wind measurement needs such as complex terrain wind fields, wind turbine wakes, offshore remote virtual wind towers, and three-dimensional distribution of atmospheric pollutants [22,23]. Additionally, virtual lidar can effectively complement and enhance the datasets for AI models related to CDWL [24].

The commonly used methods for generating virtual wind lidar include weighted average method [25], frequency-domain analysis method [20], and time-domain analysis method [26], each with its own advantages and disadvantages. While the weighted average method is simple to implement and fast in computation, it does not fully consider the lidar hardware parameters, the stochastic nature of atmospheric phase, and the process of lidar signal acquisition and processing, leading to discrepancies between the detection results of virtual lidar and real lidar. On the other hand, the frequency-domain analysis method and time-domain analysis method, although more accurate and reliable, have a significantly increased computational load. As a result, simulation speed decreases substantially, making them unsuitable for applications that require high real-time performance.

This study aims to explore the impact of lidar range resolutions on wind field detection performance using virtual lidar. The structure of the paper is as follows: Section 2 introduces three virtual lidar generation methods. Section 3 introduces a dimensionless parameter for assessing wind speed errors across various range resolutions and wind scales, and combines image similarity metrics to analyze detection performance of building wake flow. Finally, a conclusion is drawn in Section 4.

2. Methods

This paper investigates three virtual lidar generation methods: the direct averaging method, the energy weighting method, and the time-domain analysis method. In the direct averaging method, the retrieved wind speed at the radial position of each range gate v_i^a is obtained by calculating the arithmetic mean of the reference wind speed within the range of each range gate. The expression is as follows:

$$v_i^a = \frac{1}{m_2 - m_1} \sum_{j=m_1}^{m_2} v_j^r \tag{1}$$

where i represents the serial number of range gates within the detection range at the lidar range resolution interval. m_1 and m_2 represent the serial numbers of the reference wind speed at the start and end points of range gate i, respectively. v_j^r represents the reference wind speed at the radial position r_j, which is derived from actual measurement or theoretical value. The atmospheric wind field is a complex nonlinear system influenced by a variety of factors, characterized by inhomogeneity and abrupt changes, which makes accurate modeling of the atmospheric wind field difficult. However, based on the statistical laws and Fourier analysis methods of the atmospheric wind field, the wind can be regarded as a waveform composed of sinusoidal wind speeds with different amplitudes and wavelengths [27]. Based on this assumption, this study obtains the radial wind speed data of the atmospheric wind field using the ideal sine wind speed model, which is expressed as:

$$v_j^r = A \cdot \sin\left(\frac{2\pi}{L} \cdot \mathrm{r}_j\right) \tag{2}$$

where j represents the serial number separated by the slice thickness Δr within the detection range, A denotes the wind speed amplitude, and L represents the reference wind speed wavelength, reflecting the characteristic scale of wind field. In practical applications, the characteristic scale is related to factors like underlying surface properties and meteorological conditions.

Optics EXPRESS

The energy weighting method considers the relationship between the range resolution of CDWL and the full width at half maximum (FWHM) of the emitted laser pulse. Assuming a Gaussian shape for the laser pulse, a power simulation model for the lidar pulse signal at each range gate is established. The expression is as follows:

$$P_i = \frac{2\sqrt{\ln 2}}{\sqrt{\pi}\cdot\Delta R}\exp(-4\ln 2(\frac{r_j - R_i}{\Delta R})^2) \tag{3}$$

where ΔR represents the lidar range resolution. Based on the power simulation results from Eq. (3), the retrieved wind speed at the radial position of each range gate v_i^e is obtained by the energy-weighted average of the reference wind speed within the range of each range gate. The expression is as follows:

$$v_i^e = \frac{\sum_{j=m_3}^{m_4} v_j^r P_i}{\sum_{j=m_3}^{m_4} P_i} \tag{4}$$

The time-domain analysis method divides the aerosol scatterers within the detection range into slices of equal thickness along the light beam propagation axis. The aerosol particles within each slice have the same speed and direction of motion, and the scattering coefficient is constant. Due to the random distribution and irregularity of the scatterers, the phase and amplitude of the scattered light waves change. When these scattered light waves coherently superimpose in space, they form a random pattern of fine bright and dark spots on the receiving surface, known as speckle phenomenon [28]. To simulate a more realistic atmospheric echo signal, this method takes the speckle phenomenon into account, thereby obtaining the heterodyne current signals for each layer. By stacking and splicing the echo signals of each layer in time sequence, the time-domain model of the echo signals within the effective detection range is formed [26]:

$$\begin{aligned} &i(t) = 2\Re\exp(j2\pi v_M t_j)\times \\ &\textstyle\sum_N a_j[\eta_s P_{LO} P_T(\mathrm{t_j} - 2r_j/c)T^2(r_j)\beta(r_j)\Delta r(A_r/r_j^2)]^{1/2}\exp(-j2kv_j^r t_j) \end{aligned} \tag{5}$$

where $i(t)$ represents the heterodyne current at time t within the range gate, v_M is the AOM frequency shift, t_j is the sampling time of the atmospheric wind field node j, P_{LO} is the local oscillator light power, η_s is the total optical efficiency of the system, c is the speed of light, A_r is the receiving area of the telescope, k is the wave number of the laser emitted by the virtual wind measuring lidar, and a_j is the random factor corresponding to the speckle effect of the echo signal. N is the total number of nodes between two atmospheric wind field nodes within the detection range with the slice thickness Δr. $T(r_j)$ and $\beta(r_j)$ represent the transmittance and backscattering coefficient at the radial position r_j, respectively. Subsequently, by performing a Fast Fourier Transform (FFT) on the heterodyne current, the power spectrum within each range gate is obtained. The retrieved wind speed at the radial position of each range gate can be determined by spectrum analysis. The pulse accumulation number is set to 100 to balance computational complexity and signal quality [29]. The specific lidar simulation parameters are listed in Table 1.

3. Results and discussion

3.1. Comparison of the three virtual lidar generation methods

The measured data from a 0.9-m high-resolution CDWL is adopted as the reference wind speed. The 0.9-m high-resolution CDWL employed pseudorandom phase modulation (PRM) technology to achieve sub-meter resolution, which was validated through comparative analysis with conventional pulsed CDWL. It was proved to be able to capture the meter-scale perturbation wind from an electric fan in the experiment [30]. The results of the direct averaging method,

Optics EXPRESS

the energy weighting method, and the time-domain analysis method are compared with the measured data in Fig. 1. The real atmospheric wind field is characterized by irregularities and stochastic variations over time, primarily due to atmospheric turbulence and convective activities. These characteristics result in fluctuations in the wind field across a spectrum of frequencies and intensities.

Table 1. The lidar simulation parameters

Parameter	Value	Unit
Laser wavelength	1550	nm
Transmitted pulse energy	100	μJ
Sampling frequency	250	MHz
Telescope diameter	80	mm
Local oscillator light power	0.1	mW
Backscattering coefficient	8×10^{-6}	$m^{-1} sr^{-1}$
Atmospheric transmittance	0.8	-

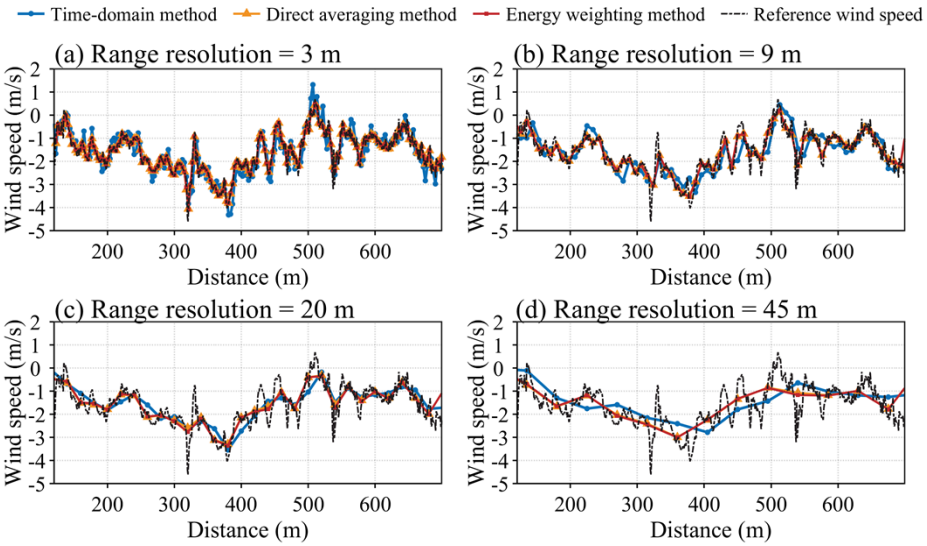

Fig. 1. Wind field retrieval results of virtual lidar with various range resolutions using three methods. The reference wind speed is derived from 0.9 m range resolution CDWL data.

The wind speeds retrieved by the direct averaging method and the energy weighting method are highly consistent, when compared to the wind field retrieval results of the three virtual lidar generation methods. This consistency stems from the fact that both methods employ the weighted average approach. The subtle difference is due to the difference of weighting factors. These weighted average approaches reduce the impact of random fluctuations in the wind field, resulting a smoother result compared to the reference wind speed. These methods are relatively faster in calculation and closer to the reference wind field compared to the time-domain analysis method. However, they fail to fully consider the lidar hardware parameters, the stochastic nature of atmospheric phase, and the process of lidar signal acquisition and processing. As a result, there is a discrepancy between the results of virtual lidar retrieval and real lidar detection, leading to lower reliability. In contrast, the time-domain analysis method is more reliable in reflecting the real lidar detection performance because it more thoroughly considers the various aspects

Optics EXPRESS

of real lidar detection. However, this method leads to a significant increase in computational load, which substantially slows down the simulation speed and results in relatively poor real-time performance.

In addition, a higher range resolution is superior in capturing the nuanced dynamics of the wind field with greater precision and sensitivity, as shown in Fig. 1(a). In contrast, lower range resolution attenuates the responsiveness to rapid changes in wind speed. This can lead to underestimation and misalignment of wind speed extremes, as shown in Fig. 1(d). These insights underscore the pivotal importance of range resolution in ensuring the precision and dependability of wind speed measurements.

To further investigate the relationship between range resolution and wind field scale, the sinusoidal reference wind field is applied. Figure 2 shows the retrieval results of three virtual lidar generation methods for various wind characteristic scales at a range resolution of 30 m. In Fig. 2(a), when the wind field scale is twice the range resolution, the wind field retrieval results of the direct averaging method and the energy weighting method tend to zero, and the wind speed extremes cannot be captured. Although the time-domain analysis method can capture the extremes, their position does not match those of the reference wind speed. In Fig. 2(b), when the wind field scale is three times the range resolution, the wind speed retrieved by the three methods matches the reference wind speed. However, the wind speed extremes are slightly underestimated and misaligned. In Fig. 2(c) and (d), when the wind field scale is 8 times and 16 times of the range resolution respectively, the wind speed retrieved by the three methods is highly consistent with the reference wind speed. This indicates that a 30-m range resolution can effectively detect such structures.

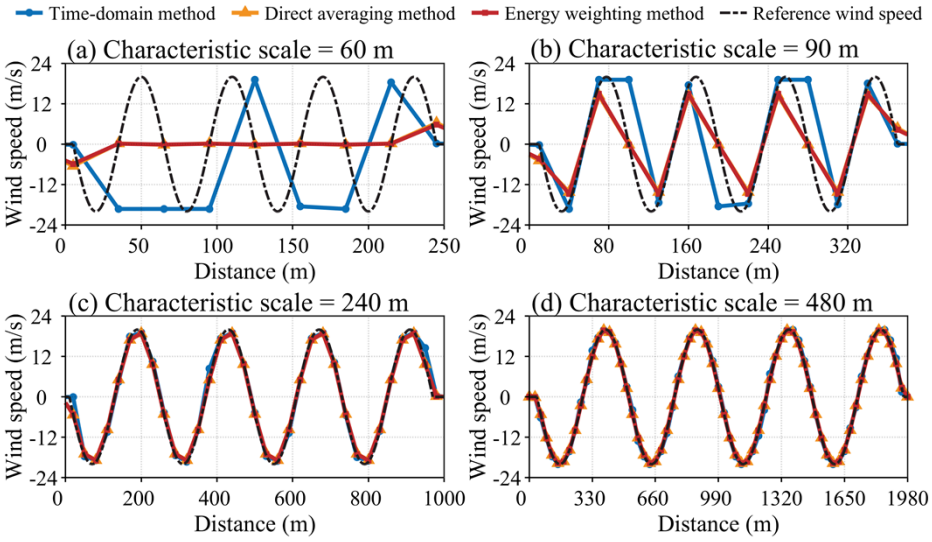

Fig. 2. Wind field retrieval results of virtual lidar with various characteristic scales using three methods. The range resolution is 30 m.

3.2. *Error assessment of wind field retrieval*

Both the range resolution of lidar and the scale of the wind field affect lidar detection performance. To quantify how different range resolutions impact the detection performance of various wind field scales, three error metrics are employed to assess the wind field retrieval effectiveness. These metrics include Root Mean Square Error (RMSE), Mean Relative Error (MRE), and Mean Absolute Error (MAE). These metrics compare the wind speeds retrieved by the virtual lidar

Optics EXPRESS

with the reference wind speeds. RMSE is sensitive to large errors. A higher RMSE indicates greater fluctuation in the retrieval errors. MRE is suitable for comparing data of different scales, as it quantifies the relative deviation ratio of retrieved values to references. MAE does not overly amplify the impact of outliers, thus providing a balanced assessment of overall error. A single metric or combination can be selected according to the needs of the actual application scenarios.

Figure 3 illustrates the error assessment results of the virtual lidar using the time-domain analysis method. Lower lidar range resolutions and shorter characteristic scales of reference wind speeds are associated with higher errors. This increase in errors leads to a decreased ability to accurately capture the wind field. The RMSE exceeds 20 m/s when the range resolution is below 40 m at wind characteristic scale of 60 m. When the range resolution is improved to approximately 6 m, further increases in range resolution do not reduce errors. In fact, the figure shows that excessively high range resolution can slightly increase error, despite the general trend that higher resolution typically leads to smaller errors. It is because when the range resolution is too high, it leads to a significant increase in the spectral width of the signal. Insufficient pulse accumulation in the simulation also increases the errors of the results. These factors can adversely affect the accuracy of the retrieval results. This is also one of the challenges in developing single-pulse high-resolution lidar systems.

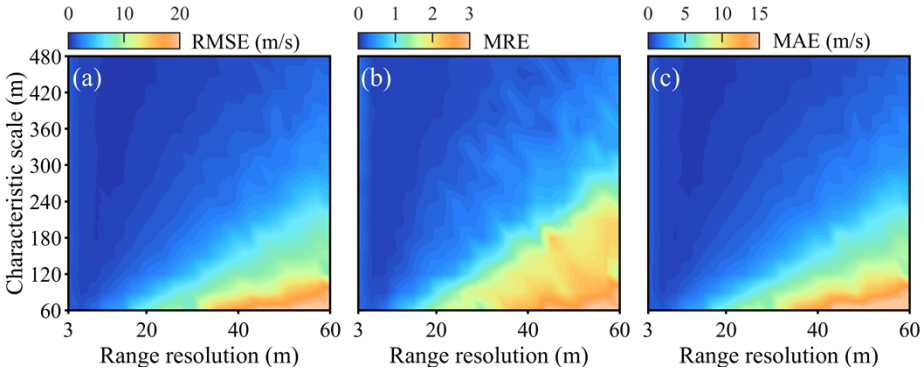

Fig. 3. Error distribution of wind speed retrieved by virtual lidar using the time-domain analysis method: (a) RMSE, (b) MRE, and (c) MAE. Range resolution varies from 3 m to 60 m. Characteristic scale ranges from 60 m to 480 m.

Wind field detection performance cannot be determined solely by the range resolution of the lidar. In Fig. 3(a), at a range resolution of 30 m, the RMSE is 0.8 m/s for a reference wind characteristic scale of 300 m. Upon increasing the characteristic scale to 60 m, the RMSE escalates to 8.1 m/s. To decouple the relationship between range resolution and wind scale, a dimensionless parameter γ is proposed. This parameter is defined as the ratio of the characteristic scale of reference wind speed to lidar range resolution. The fitting relationships between this parameter and error metrics are established based on the three virtual lidar generation methods, as shown in Fig. 4.

As the parameter increases, the error values decrease exponentially. For γ above 9.1, the RMSE of the three methods is less than 1 m/s, as shown in Fig. 4(a). According to Fig. 4(b), exceeding a γ value of 10.2 results in an MRE below 0.2 for the three methods. For γ exceeding 7.5, the MAE of the three methods is under 1 m/s, as depicted in Fig. 4(c). In this case, the range resolution does not cause large errors, thereby enabling the lidar to accurately retrieve wind speed. Additionally, when the error curves of the direct average method and the energy weighted method are close to those of the time-domain analysis method, the three methods have the same performance in lidar detection simulations. Therefore, the direct averaging method or the energy

Optics EXPRESS

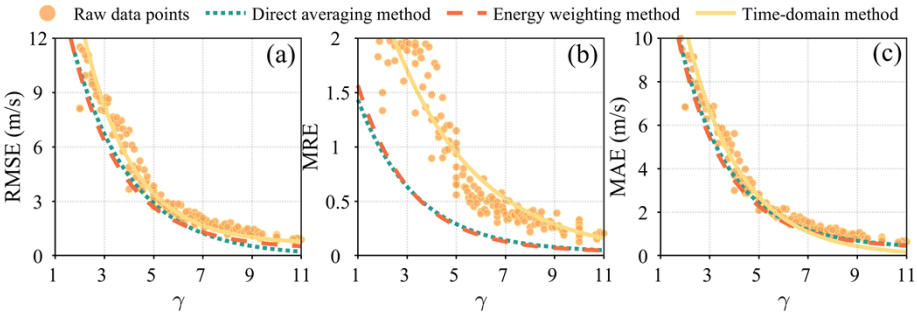

Fig. 4. The error fitting curves between RMSE, MRE, MAE and the γ based on three virtual lidar generation methods. The raw data points are the errors of wind speed retrieved by time-domain analysis method.

weighting method can replace the time-domain analysis method to generate virtual lidar. It can not only reduce the computational load and improve real-time performance but also ensure the reliability of virtual lidar retrieval.

When γ is small, the errors of the three virtual lidar generation methods are all large. The wind speed retrieved by the virtual lidar shows a significant difference from the reference wind speed. The gaps between the error fitting values of the three virtual lidar generation methods are widening. It is worth considering whether the direct averaging method or the energy weighting method can effectively simulate real lidar detection. Setting a threshold based on the actual scenario can address this issue. When the gap of error fitting values between the time-domain analysis method and the other methods exceeds the preset threshold, only the time-domain analysis method can be used. Conversely, more computationally efficient methods can be employed instead.

3.3. *Optimization of the time-domain analysis method*

As revealed by the analysis of Sec. 3.2, only the time-domain method can accurately simulate the detection performance of real lidar at a small γ. However, this method suffers large computational load, making it essential to optimize its computational efficiency. Based on Eq. (5), apart from the influence of computer hardware performance and algorithm implementation efficiency, the slice thickness Δr is a key factor. The augmentation of the slice thickness leads to a reduction in matrix size, thereby enhancing computational efficiency. Therefore, an analysis is conducted on how varying slice thickness affect the accuracy of wind field retrieval and the calculation time, as show in Fig. 5. The wind field scale is set to 240 m for different range resolutions.

Figure 5 shows how time and RMSE change with slice thickness at two range resolutions using a wind characteristic scale of 240 m. The RMSE compares the wind speed retrieved by virtual lidar with a slice thickness of 0.3 m to that with other slice thicknesses, under the same characteristic scale of reference wind speed. Time decreases rapidly as the slice thickness increases, then levels off. At a range resolution of 30 m, the value of γ corresponds to 8. Increasing the slice thickness does not substantially affect the error of wind speed retrieval, as shown in Fig. 5(a). It can expand the slice thickness without compromising the accuracy of wind speed retrieval, which leads to a significant reduction in calculation time and an improvement in real-time capabilities. However, at a range resolution of 60 m, the value of γ corresponds to 4. Increase in slice thickness can result in a considerable rise in wind speed retrieval error, as shown in Fig. 5(b). It requires more caution to avoid significant accuracy loss. For example, if RMSE does not exceed 3 m/s, the slice thickness should be controlled within 4 m in the case of Fig. 5(b). Incidentally, the relationship between RMSE and slice thickness is also influenced

Optics EXPRESS

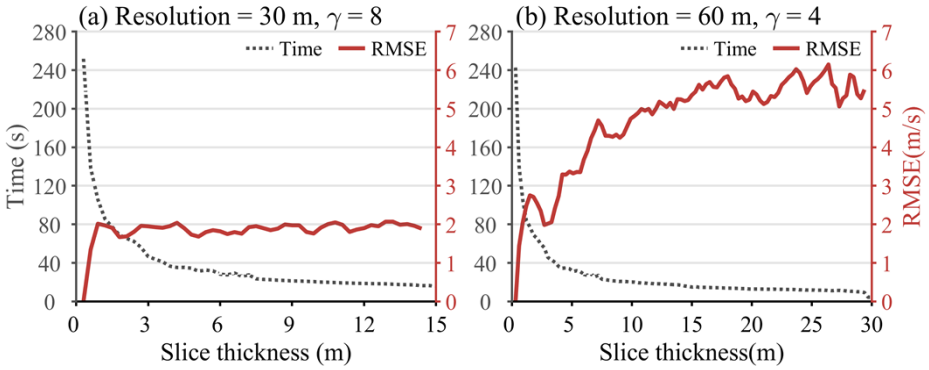

Fig. 5. The RMSE and calculation time of virtual lidar using the time-domain analysis method with a range resolution of 30 m and 60 m respectively. The characteristic scale of reference wind speed is set to 240 m. Slice thickness varies from 0.3 m to one third of the range resolution. The solid line represents RMSE. The dashed line represents the consuming time required for the computer to complete simulation calculation.

by the characteristic scale of the reference wind speed. Increasing slice thickness may not raise error much when characteristic scale is sufficiently large at 60 m range resolution.

3.4. *Application of typical building wake flow*

A typical building wake flow is constructed to evaluate the capture capability of lidar with different range resolutions for complex wind fields. The size of a single urban building is generally on the order of tens of meters. In the field of building aerodynamics, a square-shaped model is commonly used to study wind field characteristics. Therefore, a square-shaped building model with dimensions of 30 m × 30 m is constructed. The inflow velocity is set to a uniform westerly wind of 10 m/s. Through computational fluid dynamics (CFD) technology, the raw wind field is established with a grid interval of 0.18 m. A virtual lidar is placed at the air wake region of the building. While two-dimensional (2-D) wind vector field retrieval offers richer information, it introduces extra retrieval errors. Notably, errors from range resolution will amplify the extra errors introduced by the 2-D retrieval algorithm. Low range resolution leads to an increase in radial errors and a degradation in wind texture capture, thereby compounding wind direction inaccuracies. It's hard to distinguish errors from range resolution and those from different 2-D retrieval algorithms. Therefore, this application focuses on the impact of range resolutions on radial wind velocity. Fortunately, radial wind speed is the projection of wind vectors onto beam directions, which contains vector information to some extent.

Figure 6(a) illustrates the wind speed field in the air wake region of the building. When the airflow passes over the building, vortices alternately form and shed on both sides due to the building's blocking effect. This leads to abrupt changes and instability in the wind speed. The size of the vortex shedding is related to the incoming flow velocity, and the building's windward width. The precise capture of these fine-scale structures is crucial for alerting wind shear and optimizing low-altitude flight paths, with the rapid development of low-altitude aviation economy [31–34].

Figure 6(b) shows the result of projecting the raw wind field onto the radial wind field, which is set as reference wind field. Figures 6(c)-(e) depict the retrieved radial wind field of virtual lidar at different range resolutions with time-domain analysis method. The retrieval range is within 500 m around the virtual lidar. Angular scan increment is 0.25° to eliminate the influence of tangential resolution on the results.

Optics EXPRESS

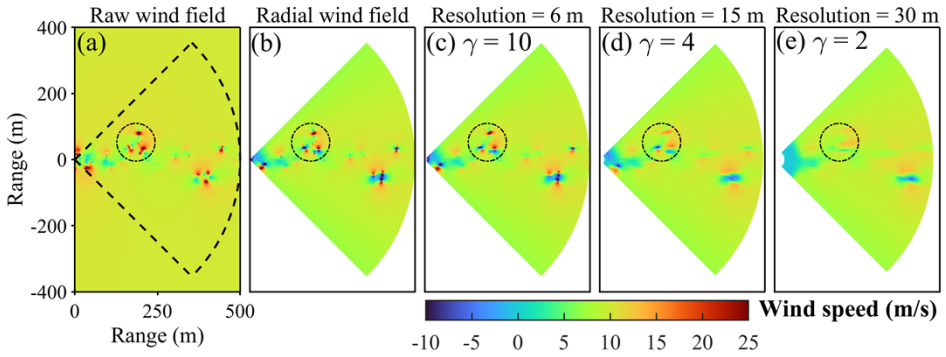

Fig. 6. (a) shows the raw wind field of a typical building wake flow. (b) shows the radial wind field centered on the virtual lidar. (c)-(e) show wind field retrieval results of virtual wind lidar with different range resolutions using time-domain analysis method. The range resolutions are 6 m, 15 m, and 30 m, respectively.

In the black circular area of raw wind field, the sudden shifts in color blocks of radial wind speed indicate the presence of variable vortices. The wind scale of this area is approximately 60 m, as shown in Fig. 6(b). The range resolution of 6 m corresponds to the γ of 10. The abrupt changes in wind speed can be well depicted, including the magnitudes and locations of these changes, as shown in Fig. 6(c). As the range resolution is decreased to 15 m, the corresponding value of γ becomes 4. The magnitudes of the abrupt changes of retrieved wind speed decrease, and a certain degree of misalignment occurs, as illustrated in Fig. 6(d). The range resolution of 30 m corresponds to the γ of 2. These abrupt wind changes in the circle area cannot be effectively retrieved, as shown in Fig. 6(e). The lower range resolution of lidar, the fewer details of the wind field it can detect, which leads a significant decrease in the accuracy of wind speed retrieval.

To comprehensively evaluate the retrieval effects of virtual lidar under three different range resolutions, the evaluation is carried out from dual perspectives. RMSE and Peak-to-Peak Relative Error (PPRE) are adopted to evaluate the accuracy of wind speed retrieval. PPRE provides a measure of peak wind speed capture capability, which is helpful to evaluate the capture ability of wind shear intensity in practical applications. The Peak Signal-to-Noise Ratio (PSNR), Structural Similarity Index (SSIM), Visual Information Fidelity (VIF) are adopted to evaluate the ability to depict the textural features of wind field [24,35]. PSNR quantifies the absolute accuracy of pixel values, directly reflecting wind speed deviations at each grid point. A high PSNR suggests that the wind speed at each point in the retrieved wind field closely matches the reference values. SSIM assesses similarity in luminance, contrast, and structural patterns within local windows. A high SSIM implies a high degree of similarity in the structural characteristics of local zones relative to the reference values. VIF models the human visual system, quantifying perceptually retained details. A VIF approaching 1 indicates the retrieved wind field retains rich, visually discernible details, such as small vortices and complex turbulent patterns. The primary metric should align with the specific wind field evaluation objective.

The values of each metrics under different range resolutions are shown in Table 2. The RMSE increases from 1.01 m/s to 2.89 m/s, signifying a rise in the error of wind speed retrieval. Due to the relatively stable wind speed in most scanning areas, the overall RMSE is not very large. However, for vortex shedding regions, the wind field scale is small and the peak wind speed is large. These resolutions not fully capture peak values, resulting in a greater error in vortices region. Specifically, the PPRE escalates from 13.26% to 53.56%, indicating a decline in the ability to capture peak wind speed. Despite PPRE reaches 25.49% at range resolution of 15 m, the vortex shedding structure can still be identified in the image. The image similarity metrics

Optics EXPRESS

can evaluate the impact of different range resolution on vortex shedding structures. A discernible trend of degradation in image similarity is observed with the decrease in range resolution. This is demonstrated by a decline in PSNR from 28.99 dB to 23.88 dB, a reduction in VIF from 0.53 to 0.19, and the SSIM which drops from 0.97 to 0.93. Furthermore, the sensitivity of image similarity metrics in key regions can be improved through region segmentation methods.

Table 2. The values of each evaluation metric under different range resolutions

Range resolution (m)	RMSE (m/s)	PPRE	PSNR (dB)	VIF	SSIM
6	1.01	13.26%	28.99	0.53	0.97
15	1.86	25.49%	25.32	0.42	0.95
30	2.89	53.56%	23.88	0.19	0.93

For practical lidar systems, indiscriminately enhancing the range resolution can lead to a substantial increase in hardware costs and technical complexity. The high-resolution lidar also faces pulse crosstalk, spectrum broadening, longer accumulation time and poor stability of pulse coding system. In extreme scenarios, even with the improved range resolution, the lidar may still fail to accurately capture the magnitude of peak wind speeds. However, based on image similarity metrics, an optimal range resolution can be identified. This ensures that the lidar can capture the textural features of the wind field, which is particularly useful for identifying wind shear. Achieving this balance is crucial for optimizing lidar system performance, as it involves finding the optimal trade-off among range resolution, cost, and detection capability.

4. Conclusion

This study analyzes the impact of range resolutions on wind field detection performance using virtual lidar. Insufficient range resolution can cause underestimation and misalignment of peak wind speeds. A dimensionless parameter γ is proposed to decouple the relationship between range resolution and wind field scale. Results indicate that when γ exceeds 9, all the three virtual lidar generation methods perform similarly, allowing for the use of computationally efficient averaging methods. Conversely, when γ is small, the averaging methods tend to underestimate the wind speed, requiring more accurate time-domain analysis method. By establishing the fitting relationship between γ and error metrics, this study provides a scientific basis for selecting the best virtual lidar generation method for different scenarios. To solve the high computational load associated with the time-domain analysis method, this study optimizes computational efficiency by adjusting the slice thickness. In the application of the typical building wake flow, the performance of different range resolutions to capture vortex structures is evaluated. Additionally, this study proposes an approach based on image similarity metrics to assess the capability of different range resolutions in capturing wind field texture structures. It offers a new perspective for analyzing the impact of range resolutions on wind shear region detection.

In practical applications, the implementation of high-resolution lidar is often constrained by significant technical challenges. Therefore, it is crucial to balance the lidar's ability to capture wind field texture structures and its capacity to resolve real wind speeds. This balance is essential for selecting an optimal range resolution that maximizes detection performance while minimizing requirements of lidar hardware. This study provides a basis for lidar error assessment and range resolution selection. It offers valuable references for the application of lidar in low-altitude aviation economy, wind energy development, and civil aviation safety. This study primarily focuses on the wind field detection performance of single-pulse CDWL. The researches methods and conclusions remain applicable to direct detection wind lidar. The only difference lies in their theory of generating virtual lidar. Future work will concentrate on the simulation of high-resolution lidar systems based on complex pulse coding and modulation techniques.

Optics EXPRESS

Funding. National Natural Science Foundation of China (42405137); Natural Science Foundation of Jiangsu Province (BK20230434); Chinese Aeronautical Establishment (202300220R2001).

Acknowledgments. The authors thank Yunpeng Zhang for his guidance in lidar simulation.

Disclosures. The authors declare no conflicts of interest.

Data availability. Data underlying the results presented in this paper are not publicly available at this time but may be obtained from the authors upon reasonable request.

References

1. P. W. Chan, "Severe wind shear at Hong Kong International Airport: climatology and case studies," Meteorol. Appl. **24**(3), 397–403 (2017).
2. X. Huang, J. F. Zheng, Y. Z. Che, *et al.*, "Evolution and Structure of a Dry Microburst Line Observed by Multiple Remote Sensors in a Plateau Airport," Remote Sens. **14**(15), 3841 (2022).
3. H. W. Zhang, S. H. Wu, Q. C. Wang, *et al.*, "Airport low-level wind shear lidar observation at Beijing Capital International Airport," Infrared Phys. Technol. **96**, 113–122 (2019).
4. L. Thobois, J. P. Cariou, and I. Gultepe, "Review of Lidar-Based Applications for Aviation Weather," Pure Appl. Geophys. **176**(5), 1959–1976 (2019).
5. M. Sommerfeld, C. Crawford, A. Monahan, *et al.*, "LiDAR-based characterization of mid-altitude wind conditions for airborne wind energy systems," Wind Energy **22**(8), 1101–1120 (2019).
6. G. J. Koch, J. Y. Beyon, E. A. Modlin, *et al.*, "Side-scan Doppler lidar for offshore wind energy applications," J. Appl. Remote Sens. **6**(1), 063562-1 (2012).
7. Z. Liu, J. F. Barlow, P.-W. Chan, *et al.*, "A Review of Progress and Applications of Pulsed Doppler Wind LiDARs," Remote Sens. **11**(21), 2522 (2019).
8. C. Wang, M. J. Jia, H. Y. Xia, *et al.*, "Relationship analysis of $PM_{2.5}$ and boundary layer height using an aerosol and turbulence detection lidar," Atmos. Meas. Tech. **12**(6), 3303–3315 (2019).
9. T. W. Wei, H. Y. Xia, J. J. Hu, *et al.*, "Simultaneous wind and rainfall detection by power spectrum analysis using a VAD scanning coherent Doppler lidar," Opt. Express **27**(22), 31235–31245 (2019).
10. Z. X. Luo, X. Q. Song, J. P. Yin, *et al.*, "Comparison and Verification of Coherent Doppler Wind Lidar and Radiosonde Data in the Beijing Urban Area," Adv. Atmos. Sci. **41**(11), 2203–2214 (2024).
11. M. G. Zhao, Z. B. Yu, M. P. Li, *et al.*, "A Novel Image Preprocessing Algorithm for Doppler Wind Spectrum Inversion: Principle, Method, and Performance," IEEE Trans. Geosci. Remote Sensing **63**, 1–12 (2025).
12. C. Wang, H. Xia, Y. Wu, *et al.*, "Meter-scale spatial-resolution-coherent Doppler wind lidar based on Golay coding," Opt. Lett. **44**(2), 311–314 (2019).
13. O. Kliebisch, H. Uittenbosch, J. Thurn, *et al.*, "Coherent Doppler wind lidar with real-time wind processing and low signal-to-noise ratio reconstruction based on a convolutional neural network," Opt. Express **30**(4), 5540–5552 (2022).
14. Y. Ren, X. Wu, F. Tao, *et al.*, "Effect of Peak Power and Pulse Width on Coherent Doppler Wind Lidar's SNR," Instrumentation **2**, 26–32 (2022).
15. R. K. Newsom, W. A. Brewer, J. M. Wilczak, *et al.*, "Validating precision estimates in horizontal wind measurements from a Doppler lidar," Atmos. Meas. Tech. **10**(3), 1229–1240 (2017).
16. D. P. Held and J. Mann, "Comparison of methods to derive radial wind speed from a continuous-wave coherent lidar Doppler spectrum," Atmos. Meas. Tech. **11**(11), 6339–6350 (2018).
17. G. Marseille and A. Stoffelen, "Simulation of wind profiles from a space-borne Doppler wind lidar," Quart. J. Royal. Meteoro. Soc. **129**(594), 3079–3098 (2003).
18. D. Conti, V. Pettas, N. Dimitrov, *et al.*, "Wind turbine load validation in wakes using wind field reconstruction techniques and nacelle lidar wind retrievals," Wind Energ. Sci. **6**(3), 841–866 (2021).
19. P. Gasch, A. Wieser, J. K. Lundquist, *et al.*, "An LES-based airborne Doppler lidar simulator and its application to wind profiling in inhomogeneous flow conditions," Atmos. Meas. Tech. **13**(3), 1609–1631 (2020).
20. V. A. Banakh and C. Werner, "Computer simulation of coherent Doppler lidar measurement of wind velocity and retrieval of turbulent wind statistics," Opt. Eng. **44**(7), 071205 (2005).
21. C. Rahlves, F. Beyrich, and S. Raasch, "Scan strategies for wind profiling with Doppler lidar - an large-eddy simulation (LES)-based evaluation," Atmos. Meas. Tech. **15**(9), 2839–2856 (2022).
22. F. Carbajo Fuertes and F. Porté-Agel, "Using a virtual lidar approach to assess the accuracy of the volumetric reconstruction of a wind turbine wake," Remote Sens. **10**(5), 721 (2018).
23. R. Robey and J. K. Lundquist, "Influences of lidar scanning parameters on wind turbine wake retrievals in complex terrain," Wind Energ. Sci. **9**(10), 1905–1922 (2024).
24. H. Y. Yang, J. L. Yuan, L. Guan, *et al.*, "Reconstruction for beam blockage of lidar based on generative adversarial networks," Opt. Express **32**(8), 14420–14434 (2024).
25. E. Simley, L. Y. Pao, R. Frehlich, *et al.*, "Analysis of light detection and ranging wind speed measurements for wind turbine control," Wind Energy **17**(3), 413–433 (2014).
26. P. Salamitou, A. Dabas, and P. H. Flamant, "Simulation in the time domain for heterodyne coherent laser radar," Appl. Opt. **34**(3), 499–506 (1995).
27. Y. Zhou, L. Li, K. Wang, *et al.*, "Coherent Doppler wind lidar signal denoising adopting variational mode decomposition based on honey badger algorithm," Opt. Express **30**(14), 25774–25787 (2022).

Optics EXPRESS

28. J. W. Goodman, "Statistical properties of laser speckle patterns," in *Laser Speckle and Related Phenomena* (Springer, 1975), pp. 9–75.
29. F. Zhang, S. Zhang, L. Wang, *et al.*, "A probability-constraint-based method based on the honey badger algorithm for wind estimation with coherent Doppler wind lidar," Opt. Express **32**(26), 45662–45678 (2024).
30. Y. Zhang, J. Yuan, Y. Wu, *et al.*, "Sub-meter wind detection with pulsed coherent Doppler lidar," Phys. Rev. Fluids **8**(2), L022701 (2023).
31. H. Gao, C. Shen, X. Wang, *et al.*, "Interpretable semi-supervised clustering enables universal detection and intensity assessment of diverse aviation hazardous winds," Nat. Commun. **15**(1), 7347 (2024).
32. P. W. Chan, K. K. Hon, and D. K. Shin, "Combined use of headwind ramps and gradients based on LIDAR data in the alerting of low-level windshear/turbulence," Meteorologische Zeitschrift **20**(6), 661–670 (2011).
33. J. L. Yuan, H. Y. Xia, T. W. Wei, *et al.*, "Identifying cloud, precipitation, windshear, and turbulence by deep analysis of the power spectrum of coherent Doppler wind lidar," Opt. Express **28**(25), 37406–37418 (2020).
34. X. Huang, "The small-drone revolution is coming—scientists need to ensure it will be safe," Nature **637**(8044), 29–30 (2025).
35. H. R. Sheikh and A. C. Bovik, "Image information and visual quality," IEEE Trans. on Image Process. **15**(2), 430–444 (2006).